# Continuum breakdown in compressible mixing layers

Vishnu Mohan[*] and A. Sameen[†]
*Department of Aerospace Engineering, Indian Institute of Technology Madras, Chennai 600036, India*

Balaji Srinivasan[‡]
*Department of Mechanical Engineering, Indian Institute of Technology Madras, Chennai 600036, India*

Sharath S. Girimaji[§]
*Department of Ocean Engineering, Texas A&M University, College Station, Texas 77843, USA*

(Received 14 March 2022; accepted 11 May 2022; published 8 June 2022)

Gas-kinetic simulations of rarefied and compressible mixing layers are performed to characterize continuum breakdown and the effect on the Kelvin-Helmholtz instability. The unified gas-kinetic scheme (UGKS) is used to perform the simulations at different Mach and Knudsen numbers. The UGKS stress tensor and heat-flux vector fields are compared against those given by the Navier-Stokes-Fourier constitutive equations. The most significant difference is seen in the shear stress and transverse heat flux. The study demonstrates the existence of two distinct continuum breakdown regimes, one at low and the other at high convective Mach numbers. Overall, at low convective Mach numbers, the deviation from continuum stress and heat flux appears to scale exclusively with the micro-macro length scale ratio given by the Knudsen number. On the other hand, at high convective Mach numbers, the deviation depends on the global micro-macro timescale ratio given by the product of Mach and Knudsen numbers. We further demonstrate that, unlike shear stresses and transverse heat flux, the deviations in normal stresses and the streamwise heat flux depend separately on Knudsen and Mach numbers. A local parameter called the gradient Knudsen number is proposed to characterize the rarefaction effects on the local momentum and thermal transport. Noncontinuum aspects of gas-kinetic stress-tensor and heat-flux behavior that Grad's 13-moment equation model reasonably captures are identified.

DOI: 10.1103/PhysRevE.105.065102

## I. INTRODUCTION

The Navier-Stokes-Fourier (NSF) constitutive equations form the foundation of the fluid flow and thermal transport description in the continuum flow regime. However, these constitutive relations can be inadequate to describe momentum or heat transport in rarefied flows. The degree of rarefaction is typically characterized in terms of the Knudsen number Kn, which is the ratio of the mean free path of the medium $\lambda$ to the length scale of the flow $L$. The limit of vanishing Kn represents the continuum regime of fluid flow. The Knudsen number can be finite in many practical applications, and rarefaction effects become important. For example, rarefaction effects play a critical role in the free shear (mixing) layers of the slipstream behind Mach stems [1,2], exhaust plumes of satellite nozzles [3–5], and other space applications. The extent of rarefaction effects can vary with the type of flow and the Mach and Knudsen numbers. At the very extreme, rarefaction effects can manifest as anti-Fourier transport (cold to hot heat transfer) as seen in certain regions of lid-driven cavity flows [6,7]. Yet Venugopal *et al.* [6] observed that, even at large Knudsen numbers, areas of Fourier transport can coexist with regions of anti-Fourier heat transfer in cavity flows. Thus, the rarefaction effects can be complex and localized, requiring further investigation.

Various nondimensional parameters have been employed in the literature to characterize the deviation from continuum NSF constitutive equations. Bird [8] demonstrated that the continuum breakdown can be reasonably quantified in terms of a suitably normalized density gradient. A parameter $\mathrm{Ma}_c^2/\mathrm{Re}$, where $\mathrm{Ma}_c$ is the convective Mach number and Re is the Reynolds number, can be devised [8] to quantify the degree of breakdown. Tsien [9] suggested a similar nondimensional number by comparing continuum and noncontinuum parts of the Burnett equation. Upon using the relationship $\mathrm{Re} \approx \mathrm{Ma}_c/\mathrm{Kn}$, it can be seen that the above parameter is $\mathrm{Ma}_c\mathrm{Kn}$, which is shown to be equal to the ratio of the microscopic timescale to the macroscopic timescale. Ben-Ami and Manela [10] showed that for a pulsating sphere, the failure of the NSF and the regularized Grad13-moment equation [11] depend on both the nondimensional length scale (Knudsen number) and the nondimensional timescale (defined as the ratio of the frequency of pulsation to the molecular collision frequency). A local parameter was suggested by Boyd *et al.* [12], given as $\mathrm{Kn}_{GLL} = (\lambda/Q)|\nabla Q|$, where $Q$ can be either temperature or density. Tiwari [13] obtained a similar

[*]ae16d421@smail.iitm.ac.in
[†]sameen@ae.iitm.ac.in
[‡]sbalaji@iitm.ac.in
[§]girimaji@tamu.edu

 ©2022 American Physical Society

expression for the deviation from equilibrium, using a method identical to Grad's 13-moment equation method [14]. It can be seen that the above definition is similar to the conventional definition of the Knudsen number, based on the gradient of thermodynamic variables. It is also possible to directly relate $|\nabla Q|$ to the Mach number by considering compressibility effects. A common limitation of the above methods is that all these parameters show negligible values at low Mach numbers. An alternative method suggested by Lockerby *et al.* [15] uses the parameter $\mathrm{Kn}_Q = \|Q - Q^{\mathrm{NS}}\|/\|Q^{\mathrm{NS}}\|$ to assess the deviation from the NSF equation, where $Q$ is either the stress tensor or the heat-flux components obtained from the Boltzmann relationship, $Q^{\mathrm{NS}}$ is the stress or heat-flux components obtained from the NSF equation, and $\|\cdot\|$ represents the $L_2$-norm of the components. In this approach, since all the components are combined in the $L_2$-norm, only the deviation with respect to the most dominant component is highlighted. This measure does not account for the deviation of individual stress or heat-flux components and may not shed light on the underlying physics. Further, this measure can be singular in the limit of vanishing $Q^{\mathrm{NS}}$. Wang *et al.* [16] showed that the ratio of non-Fourier to Fourier parts of the heat flux can be used to identify different regimes of interaction between the bow shock and stagnation boundary layer in flow past a cylinder. Singh and Schwartzentruber [17,18] have shown that the stagnation point heat flux in hypersonic flow past a blunt body scales as $\mathrm{Ma}^{2\omega}/\mathrm{Re}$, where $\omega$ is the viscosity-temperature index, while the drag force on the body scales with $C^*\mathrm{Ma}^2/\mathrm{Re}$, as suggested by Macrossan [19].

The present study focuses on the characterization of the continuum breakdown in compressible mixing layers. Unified gas kinetic scheme (UGKS) [20] simulations of mixing layers at different Mach and Knudsen numbers are performed. The departure of the UGKS stress tensor and heat-flux components from the NSF constitutive equations is examined. Different scaling regimes are identified based on the Knudsen and Mach numbers. An important finding is that the normal and transverse stress or flux components exhibit markedly different behavior. It is demonstrated that many of the noncontinuum characteristics of momentum and thermal transport are captured reasonably well by Grad's 13-moment equations. These findings enhance our understanding of rarefaction effects in free-shear flows.

## II. KINETIC THEORY: SOLUTION AND MODELS

The particle distribution function $f(x_i, c_j, t)$ is defined such that $f(x_i, c_j, t)dc_j dx_i$ gives the number of particles within a velocity range of $c_j$ and $c_j + dc_j$ and position range of $x_i$ and $x_i + dx_i$. In the present study, this quantity is multiplied by $m$, where $m$ is the mass of a single particle. This gives the density $\rho(x_i, t)$ of the medium at a specific point when $f$ is integrated over the entire velocity space. The governing equation for $f$ is the Boltzmann transport equation, given by

$$\frac{\partial f}{\partial t} + c_i \frac{\partial f}{\partial x_i} + \frac{\partial F_i f}{\partial c_i} = C, \tag{1}$$

where $F_i$ is the external force per unit mass. The left-hand side of the equation describes the changes in the particle distribution function due to advection. The right-hand-side term $C$ (known as the collision operator) describes the changes to the particle distribution function due to collision. Subject to a series of assumptions, known as Stosszahlansatz [14], it is possible to show that $C$ is a nonlinear integral function of the particle distribution functions before and after collisions. This equation is valid for a wide range of nonequilibrium conditions. This makes the Boltzmann transport equation an integro-differential equation which is challenging to solve [21].

### A. Moderate departure from equilibrium

In the near continuum limit, the collision operator can be further simplified. Bhatnagar *et al.* [22] suggested a simplified collision operator given as $C = \nu(f_0 - f)$, where $\nu$ is the collision frequency and $f_0$ is Maxwell's equilibrium distribution function. The Bhatnagar-Gross-Krook (BGK) approximation to the Boltzmann transport equation is popular and is easier to analyze. The simplified BGK-Boltzmann equation without any external forces is given as

$$\frac{\partial f}{\partial t} + c_i \frac{\partial f}{\partial x_i} = \nu(f_0 - f). \tag{2}$$

The Maxwell equilibrium distribution function for monatomic gas is given as

$$f_0 = \rho\Big(\frac{m}{2\pi k_B T}\Big)^{3/2} \exp\Big(\frac{m}{2k_B T}(u_i - c_i)^2\Big), \tag{3}$$

where $\rho = \rho(x_i, t)$ is the density of the medium, $k_B$ is the Boltzmann constant, $T = T(x_i, t)$ is the temperature of the medium, and $u_i = u_i(x_i, t)$ is the macroscopic velocity. Since the present work concentrates on monatomic gases, the internal degrees of freedom are not considered.

The macroscopic conservative variables $W = \{\rho, \rho u_i, \rho E\}$ can be obtained from moments of $f$ with the collision invariants $\psi = \{1, c_i, c_i^2/2\}$ and is given as

$$W_\alpha = \int \psi_\alpha f \, dc_i, \tag{4}$$

where $\alpha$ refers to each of the components of $W$ and $\psi$. Further, the stress tensor $\tau_{ij}$ and heat-flux vector $q_i$ can be obtained as

$$\tau_{ij,B} = \int f(c_i - u_i)(c_j - u_j)d\vec{c} - \frac{\delta_{ij}}{3}\int f(c_k - u_k)^2 d\vec{c}, \tag{5}$$

$$q_{i,B} = \frac{1}{2}\int f(c_i - u_i)(c_k - u_k)^2 d\vec{c}, \tag{6}$$

where the subscript $B$ implies that it is obtained from $f$ by directly solving the Boltzmann transport equation. When the flow is in equilibrium, $f = f_0$, $\tau_{ij,B} = 0$, and $q_{i,B} = 0$.

On substituting $\psi$ into the Boltzmann transport equation and integrating for all possible particle velocity ranges, the governing equations for the macroscopic variables are obtained as

$$\frac{\partial \rho}{\partial t} + \frac{\partial \rho u_i}{\partial x_i} = 0, \tag{7}$$

$$\rho\frac{\partial u_i}{\partial t} + \rho u_j \frac{\partial u_i}{\partial x_j} + \frac{\partial \tau_{ij}}{\partial x_j} + \frac{\partial p}{\partial x_i} = 0, \tag{8}$$

$$C_v\rho\frac{\partial T}{\partial t}+C_v\rho u_j\frac{\partial T}{\partial x_j}+p\frac{\partial u_j}{\partial x_j}+\frac{\partial q_j}{\partial x_j}+\tau_{ij}\frac{\partial u_i}{\partial x_j}=0, \quad (9)$$

where $C_v=\frac{3}{2}R$ is the specific-heat capacity at constant volume for a monatomic gas, $p=\frac{1}{3}\int f(c_k-u_k)^2 d\vec{c}$ is the pressure, and $R=k_B/m$ is the gas constant. However, $\tau_{ij}$ and $q_i$ are unknowns in these equations, except at equilibrium. Equations of $\tau_{ij}$ and $q_i$ can be obtained by taking the moments of the Boltzmann transport equation; however, these equations also require higher-order moment terms, i.e., moments of $f$ where the integrand has higher powers of the components of $\vec{c}$. Similarly, the higher-moment equations require even higher-order moment terms; thus, an infinite set of coupled moment equations are needed, raising a closure problem. A common method to overcome this issue is to deduce a form for $f$. Two methods of deduction are discussed here: the NSF equation (using a Chapman-Enskog expansion for $f$) and Grad's 13-moment equation (using a Hermite polynomial expansion for $f$).

#### *1. Navier-Stokes-Fourier equation*

In the continuum limit, a first-order deviation from the equilibrium distribution function is sufficient to describe the development of flow in rarefied regimes. The NSF equation can be obtained by using the Chapman-Enskog expansion, in which $f$ is expanded, as shown by [21]

$$f=f_0(1+\mathrm{Kn}f_1). \quad (10)$$

On substituting this equation in the BGK-Boltzmann transport equation, neglecting terms of $O(\mathrm{Kn}^2)$, and manipulating using Eqs. (7)–(9), it is possible to show that

$$f=f_0\left(1-\frac{1}{\nu}\left[\hat{c}_i\left(\frac{\hat{c}_k^2}{2RT}-\frac{5}{2}\right)\frac{\partial}{\partial x_i}(\ln T)+\frac{\hat{c}_{<i}\hat{c}_{j>}}{RT}\frac{\partial u_i}{\partial x_j}\right]\right), \quad (11)$$

where $\hat{c}_i=c_i-u_i$ is the peculiar velocity of the particles and $\hat{c}_{<i}\hat{c}_{j>}=(\hat{c}_i\hat{c}_j+\hat{c}_j\hat{c}_i)/2-\frac{1}{3}\hat{c}_i^2\delta_{ij}$ is the traceless symmetric tensor of the product of peculiar velocities. On substituting Eq. (11) into Eqs. (5) and (6), we get that

$$\tau_{ij,\mathrm{NSF}}=-\frac{p}{\nu}\left[\left(\frac{\partial u_i}{\partial x_j}+\frac{\partial u_j}{\partial x_i}\right)-\frac{2}{3}\delta_{ij}\frac{\partial u_k}{\partial x_k}\right], \quad (12)$$

$$q_{i,\mathrm{NSF}}=-\frac{5Rp}{2\nu}\frac{\partial T}{\partial x_i}, \quad (13)$$

which have a similar form to the traditional NSF equation [23],

$$\tau_{ij,\mathrm{NSF}}=-\mu\left[\left(\frac{\partial u_i}{\partial x_j}+\frac{\partial u_j}{\partial x_i}\right)-\frac{2}{3}\delta_{ij}\frac{\partial u_k}{\partial x_k}\right], \quad (14)$$

$$q_{i,\mathrm{NSF}}=-\kappa\frac{\partial T}{\partial x_i}. \quad (15)$$

Comparison of the above equations gives that $\mu=p/\nu$ and $\kappa=\frac{5}{2}(Rp/\nu)$, leading to a Prandtl number $\mathrm{Pr}=\mu C_p/\kappa=1$, where the specific heat at constant pressure $C_p=5R/2$ for monatomic gas. Here $\mu$ is the dynamic viscosity, $\nu$ is the collision frequency, and $\kappa$ is the thermal conductivity. For continuum flows, algebraic constitutive relationships for shear and heat flux are sufficient to obtain momentum and thermal transport. Further deviation from equilibrium needs to account for history and other higher-order effects.

#### *2. Grad's 13-moment equations*

In Grad's 13-moment equations, the transport equations for shear and heat flux are considered; thus, they are valid at high degrees of rarefaction. In order to close Grad's 13-moment equations, the distribution function is assumed to have the form [14]

$$f=f_0\left(\lambda^0+\lambda_i^0\hat{c}_i+\lambda^1\hat{c}_k^2+\lambda_{ij}^0\hat{c}_{<i}\hat{c}_{j>}+\lambda_i^1\hat{c}_k^2\hat{c}_i\right), \quad (16)$$

where $\lambda_{\ldots}^{\beta}$ are 13 unknown coefficients which are obtained by taking the moments given in Eqs. (4)–(6). The final form of $f$ is then obtained as

$$f=f_0\left(1+\frac{\tau_{ij}}{2p}\frac{\hat{c}_{<i}\hat{c}_{j>}}{RT}+\frac{2}{5}\frac{q_j}{pRT}\hat{c}_j\left(\frac{\hat{c}_k^2}{2RT}-\frac{5}{2}\right)\right). \quad (17)$$

In Grad's 13-moment equations, unlike the NSF equation discussed previously, the moment equations governing $\tau_{ij}$ and $q_i$ are also evaluated from the BGK-Boltzmann equation. The higher-order moments and the moments of the collision operator are then calculated using Eq. (17). The final form of Grad's 13-moment equations for $\tau_{ij}$ and $q_i$ are [14]

$$\begin{aligned}&\frac{D\tau_{ij}}{Dt}+\frac{2}{5}\left(\frac{\partial q_i}{\partial x_j}+\frac{\partial q_j}{\partial x_i}\right)-\frac{4}{15}\delta_{ij}\frac{\partial q_k}{\partial x_k}+\left(\tau_{ki}\frac{\partial u_j}{\partial x_k}+\tau_{kj}\frac{\partial u_i}{\partial x_k}\right)\\&-\frac{2}{3}\delta_{ij}\tau_{kl}\frac{\partial u_l}{\partial x_k}+\tau_{ij}\frac{\partial u_k}{\partial x_k}+p\left(\frac{\partial u_i}{\partial x_j}+\frac{\partial u_j}{\partial x_i}\right)-\frac{2p}{3}\delta_{ij}\frac{\partial u_k}{\partial x_k}\\&=-\frac{p}{\mu}\tau_{ij},\end{aligned} \quad (18)$$

$$\begin{aligned}&\frac{Dq_i}{Dt}+\frac{5R}{2}p\frac{\partial T}{\partial x_i}+\frac{5R}{2}\tau_{ij}\frac{\partial T}{\partial x_j}-\tau_{ij}RT\frac{\partial ln\rho}{\partial x_j}-\frac{\tau_{ij}}{\rho}\frac{\partial \tau_{jk}}{\partial x_k}\\&+RT\frac{\partial \tau_{ij}}{\partial x_j}+\frac{7}{5}q_i\frac{\partial u_j}{\partial x_j}+\frac{7}{5}q_j\frac{\partial u_i}{\partial x_j}+\frac{2}{5}q_j\frac{u_j}{\partial x_i}=-\frac{2}{3}\frac{p}{\mu}q_i,\end{aligned} \quad (19)$$

where $D/Dt=\partial/\partial t+u_k\partial/\partial x_k$. Struchtrup [24,25] showed that Grad's 13-moment equation is accurate up to $O(\mathrm{Kn}^2)$ for the BGK-Boltzmann equation. On further increasing the Knudsen number, Grad's 13-moment equation is also invalid.

### B. Large departure from equilibrium

At high rarefaction, the distribution function is unrelated to the equilibrium distribution function and forms for the distribution functions, such as those shown in Eqs. (10) and (16), would not work. Moreover, the BGK-Boltzmann transport equation is not valid for significant deviations from equilibrium. Various numerical methods to simulate rarefied flows have been proposed, such as the discrete-velocity method (DVM) [26,27] or direct simulation Monte Carlo (DSMC) method [28]. The DSMC method is a stochastic method to solve the particle distribution function, which becomes computationally expensive when approaching the continuum due to the increase in the number of simulated particles and reduction in the mesh size. The DVM is a deterministic method

for the BGK-Boltzmann equation in which the advection and the collision terms are decoupled and the particle distribution function is discretized in the velocity space. The decoupling restricts the time step to be less than the molecular timescale, making it computationally expensive in the continuum regime. A variation of the DVM method, known as the unified gas-kinetic scheme [20,29], is used in the present work.

The UGKS is a finite-volume method that numerically solves the BGK-Boltzmann equation using an analytical integral solution given by Prendergast and Xu [30]. As mentioned earlier, in the UGKS, the particle distribution function is discretized in the velocity space. For simplicity, the one-dimensional UGKS is explained here. In the $j$th discrete-velocity space cell, the particle velocity $c$ ranges from $(j-1/2)\Delta c$ to $(j+1/2)\Delta c$. The particle distribution function in the cell, having physical space index $i$ and velocity space index $j$ at time step $n$, is represented as the cell averaged value

$$f(x_i, c_j, t^n) = f_{i,j}^n = \frac{1}{\Delta c \Delta x} \int_{x_{i-1/2}}^{x_{i-1/2}} \int_{c_{j-1/2}}^{c_{j+1/2}} f(x, c, t^n) dc\, dx, \tag{20}$$

where $f(x, c, t^n)$ is the continuous particle distribution at time $t^n$, $c_{j\pm1/2} = (j \pm 1/2)\Delta c$, and $x_{i\pm1/2} = (i \pm 1/2)\Delta x$. Thus, the particle distribution function is decomposed into many separate discrete distribution functions, representing the distribution function at that particular particle velocity.

For nonequilibrium conditions, the particle distribution does not follow the Gaussian distribution function given in Eq. (3) and its explicit form cannot be known with certainty in rarefied regimes. Thus the discrete form of the particle distribution function enables accurate simulation of flows in rarefied regimes. Moreover, the BGK collision operator does not accurately capture collisions at highly rarefied conditions. However, the evolution of each discrete distribution function can be suitably described using the BGK-Boltzmann equation as it spans only a small region in the velocity space [6]. Thus an analytical solution for the BGK-Boltzmann equation obtained by Prendergast and Xu [30] can be used in each discrete-velocity point. This solution has been used in a category of BGK-Boltzmann based continuum solvers, known as the gas-kinetic method (GKM) [31–34].

The UGKS can thus be thought of as an amalgamation of both the GKM and DVM. It uses discretization in velocity space, similar to the procedure in the DVM, and the flux computation uses the analytical solution of the BGK-Boltzmann equation mentioned above, identical to the GKM. The use of the analytical solution allows time steps in the UGKS to be calculated using the Courant-Friedrichs-Lewy criterion (rather than the molecular timescales), reducing the computational expense in simulating continuum flows. The discretization in velocity space provides flexibility to the particle distribution functions, enabling high-fidelity simulation in rarefied regimes.

In the UGKS, the BGK-Boltzmann transport equation is integrated over the finite velocity and physical space volume to obtain the discretized equation BGK-Boltzmann equation,

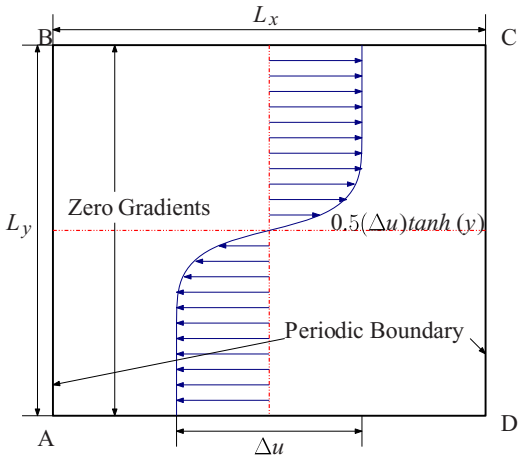


FIG. 1. Computational domain with initial velocity profile and boundary conditions.

given as [29]

$$f_{i,j}^{n+1} = f_{i,j}^n + \frac{1}{\Delta x} \int_{t^n}^{t^{n+1}} (c_j \hat{f}_{i-1/2} - c_j \hat{f}_{i+1/2}) dt + \frac{1}{\Delta x} \iint \nu (f_0 - f) dx\, dt, \tag{21}$$

where the distribution function at the cell interface is $\hat{f}$. The cell interface particle distribution function is obtained from the solution of Prendergast and Xu [30] and is given as

$$\hat{f}_{i+1/2,j}^n = \nu \int_{t^n}^{t^{n+1}} f_0(x_{i+1/2} - c_j(t-t'), t', c_j) e^{-(t-t')\nu} dt' + e^{-(t-t^n)\nu} \tilde{f}(x_{i+1/2} - c_j(t-t^n), t^n, c_j), \tag{22}$$

where $\tilde{f}$ is the particle distribution function at $t^n$. In the present work, the data obtained from the UGKS are considered the true data, and the NSF and Grad's 13-moment equations are the models considered.

The UGKS method can be summarized by the following four points.

(i) The particle distribution function is discretized in the velocity space along with the physical space and time.

(ii) The BGK approximation is valid at each discrete-velocity point.

(iii) As rarefaction increases, more discrete-velocity points are needed for high-fidelity simulation.

(iv) The macroscopic variables are calculated from the discrete particle distribution function using quadratures such as the Gauss-Hermite or Newton-Cotes quadrature.

The present work simulates a two-dimensional mixing layer to identify breakdown of the continuum hypothesis. The interpolation of the particle distribution to the cell interface uses a third-order weighted essentially nonoscillatory scheme, described by Venugopal and Girimaji [35]. The two-dimensional flow domain, initial velocity profile, and boundary conditions are shown in Fig. 1. The parameters for the present problem are the convective Mach number ($\mathrm{Ma}_c = \Delta u/2\sqrt{\gamma RT}$), Knudsen number ($\mathrm{Kn} = \lambda/\delta$), specific-heat ratio ($\gamma = 1.6667$), and Prandtl number ($\mathrm{Pr} = 1$). The Reynolds

number Re is related to $\mathrm{Ma}_c$ and Kn as

$$\mathrm{Re} = \frac{16}{5}\frac{\mathrm{Ma}_c}{\mathrm{Kn}}\sqrt{\frac{\gamma}{2\pi}}. \tag{23}$$

All the variables are nondimensionalized using the freestream temperature $T_\infty$, freestream density $\rho_\infty$, most probable speed $c_\infty = \sqrt{2RT_\infty}$, and initial vorticity thickness $\delta_0$. The mean velocity is given by $\tilde{u}(x, y) = 0.5(\Delta u)\tanh(y)$, which is seeded with harmonic ($k_x\delta_0 = 0.628$, wavelength equal to half the domain length in the streamwise direction) and subharmonic ($k_x\delta_0 = 0.314$, wavelength equal to the domain length in the streamwise direction) solenoidal perturbations [36,37].

The initial temperature distribution follows the Crocco-Busemann relationship and the pressure is kept constant throughout the domain. The initial densities of both the freestreams are equal. The particle distribution function is initialized as a Maxwellian distribution function. The grid size for all the simulations is taken to be $\Delta x/\delta_0 = 0.156\,25$ and $\Delta y/\delta_0 = 0.132\,45$, the refinement as reported in the literature [36]. The velocity space integrals are calculated using the Gauss-Hermite quadrature with 28 discretized points in the velocity space obtained by the method stated in [38]. The time step is calculated for a Courant-Friedrichs-Lewy number of 0.6 for all cases. The UGKS computations were validated in our previous paper [39]. A grid and domain independence study has been conducted for all the cases discussed here.

## III. RESULTS

The UGKS simulations for compressible mixing layers are performed for a parameter range $\mathrm{Ma}_c = 0.1$–$1.2$ and initial Knudsen number $\mathrm{Kn}_0 = 0.01$–$1.0$. The global and local deviations of the stress tensor and heat-flux vector from the NSF constitutive equation is studied. The ability of Grad's 13-moment equations to capture the variation of stress and heat flux is also tested.

The deviations are compared for various values of $\mathrm{Ma}_c$ and Kn of the mixing layer for the boundary and initial conditions discussed in Sec. II. We first discuss in this section the velocity and temperature distribution of the mixing layer for various rarefaction and compressibility regimes.

### A. Velocity and thermodynamic variable distribution

The streamwise direction $x$ is homogeneous in the computational domain at high Knudsen number since the amplitude of perturbation decays in these Knudsen number ranges, as has been shown in [39]. The distribution of velocity, temperature, and density as a function of transverse distance is analyzed for sample cases of (a) low Mach number, (b) intermediate Mach number, and (c) high Mach number.

Figures 2 and 3 show the instantaneous distribution at $t^* = \Delta u t/2\delta_0 = 10$ of $u_x$, $u_y$, $T$, and $\rho$ at $x = L_x/2$ along $y$ for $\mathrm{Ma}_c = 0.2$, 0.8, and 1.2 at $\mathrm{Kn}_0 = 1$. The width of the mixing layer (calculated using vorticity thickness $\delta = \Delta u/\omega_{\max}$, where $\omega_{\max}$ is the maximum vorticity in the flow domain) is shown by the horizontal dashed lines, with different colors representing the corresponding $\mathrm{Ma}_c$ cases. From Fig. 2(a) it can be seen that for $\mathrm{Ma}_c = 0.2$ (which is stable to Kelvin-

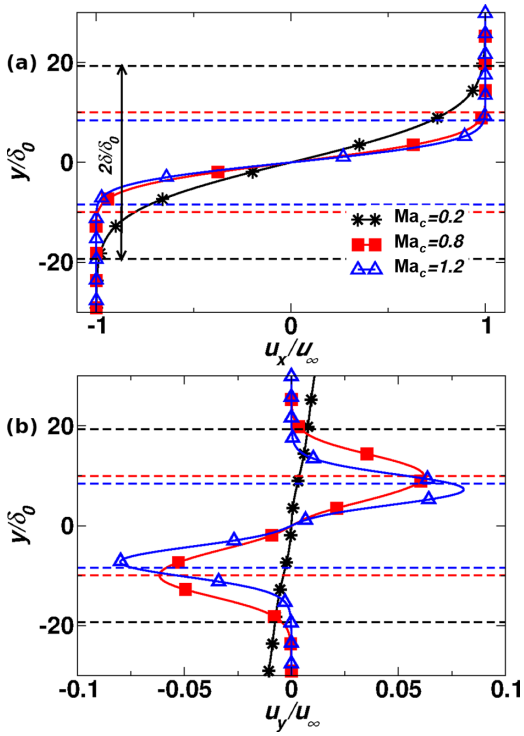


FIG. 2. Variation of (a) $u_x(x = L_x/2, y)$ and (b) $u_y(x = L_x/2, y)$ with $y$ for $\mathrm{Ma}_c = 0.2$ (black), $\mathrm{Ma}_c = 0.8$ (red), and $\mathrm{Ma}_c = 1.2$ (blue) at $\mathrm{Kn}_0 = 1.0$ and $t^* = 10$. The flow variables are normalized by the corresponding freestream values.

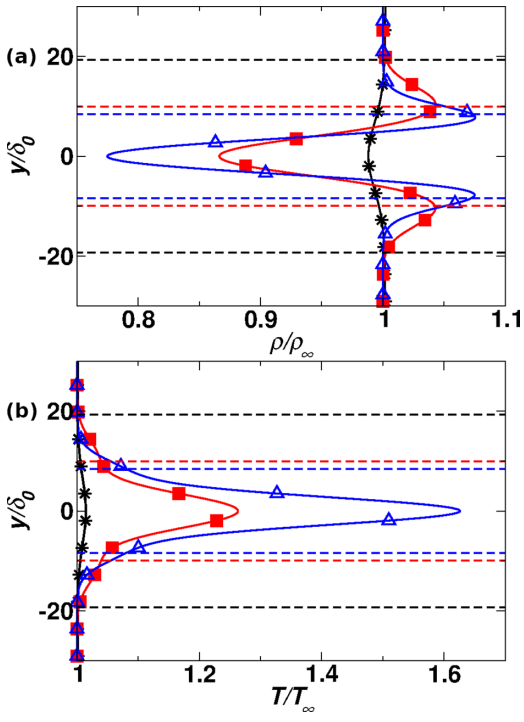


FIG. 3. Variation of (a) $\rho(x = L_x/2, y)$ and (b) $T(x = L_x/2, y)$ for $\mathrm{Ma}_c = 0.2$ (black), $\mathrm{Ma}_c = 0.8$ (red), and $\mathrm{Ma}_c = 1.2$ (blue) at $\mathrm{Kn}_0 = 1.0$ and $t^* = 10$. The flow variables are normalized by the corresponding freestream values. The legend is the same as in Fig. 2.

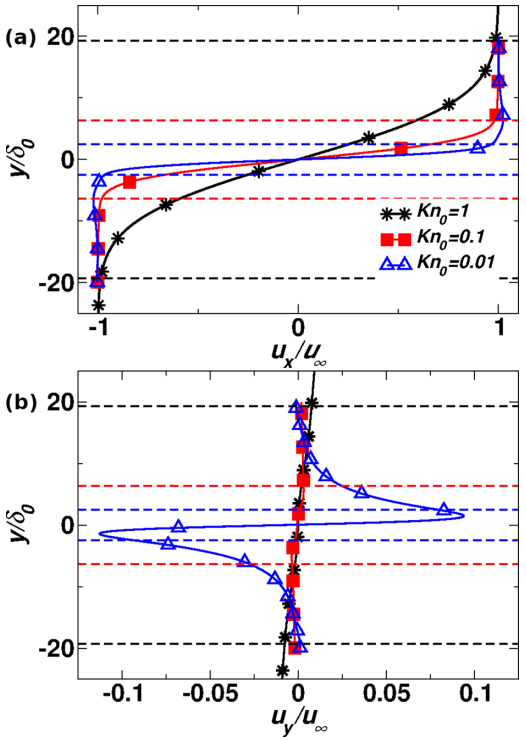


FIG. 4. Variation of (a) $u_x(x = L_x/2, y)$ and (b) $u_y(x = L_x/2, y)$ along $y$ for $\mathrm{Kn}_0 = 0.01$ (blue), $\mathrm{Kn}_0 = 0.1$ (red), and $\mathrm{Kn}_0 = 1$ (black) for $\mathrm{Ma}_c = 0.2$ and $t^* = 10$. The flow variables are normalized by the corresponding freestream values.

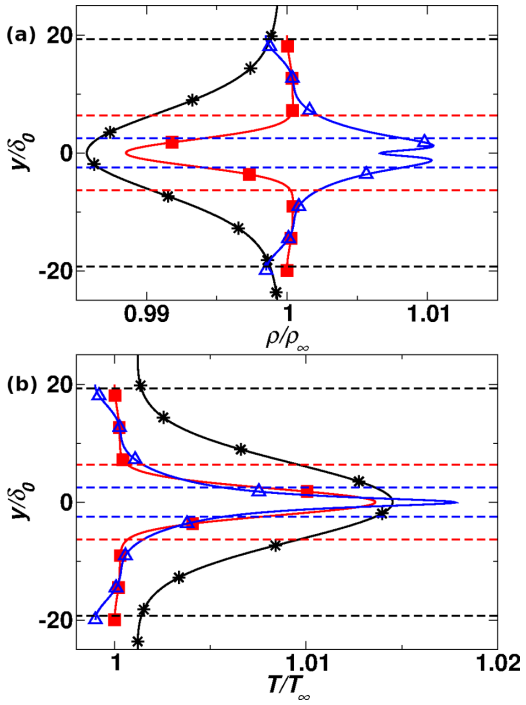


FIG. 5. Variation of (a) $\rho(x = L_x/2, y)$ and (b) $T(x = L_x/2, y)$ along $y$ for $\mathrm{Kn}_0 = 0.01$ (blue), $\mathrm{Kn}_0 = 0.1$ (red), and $\mathrm{Kn}_0 = 1$ (black) for $\mathrm{Ma}_c = 0.2$ and $t^* = 10$. The flow variables are normalized by the corresponding freestream values. The legend is the same as in Fig. 4.

Helmholtz instability), only $u_x$ shows an appreciable variation with $y$. High transverse velocity is seen in Fig. 2(b) for $\mathrm{Ma}_c = 0.8$ and 1.2 at the edge of the mixing layer. The transverse velocity diffuses as the mixing layer evolves in time. At high Mach numbers, like the transverse velocity $u_y$, significant density and temperature gradients (Fig. 3) are also seen, which are negligible at low Mach numbers. As mentioned earlier, the dashed horizontal lines indicate the mixing layer thickness, and as the Mach number increases, the mixing layer becomes thinner. The fluid tends to move away from the mixing layer center in the presence of transverse velocity. The fluid carried by $u_y$ also creates a density gradient due to mass conservation, as shown in Fig. 3(a). The density increases at the edge of the mixing layer and decreases at the center of the mixing layer. The stream velocity shows a sharp gradient at high Mach number due to the slower growth rate of the mixing layer compared to that at lower Mach number, as has been shown in [39]. Significant variation in the flow variables combined with the slower growth rate of the mixing layer thickness at high Mach numbers leads to large gradients in these flow variables.

A similar examination of the velocity, temperature, and density distribution for various $\mathrm{Kn}_0$ is shown in Figs. 4 and 5 at $\mathrm{Ma}_c = 0.2$ and in Figs. 6 and 7 at $\mathrm{Ma}_c = 1.2$. All the snapshots, as before, are taken at an instantaneous value of $t^* = 10$. In Fig. 4(a), for $\mathrm{Kn} = 0.01$, it can be seen that the peak value of $u_x$ is greater than the freestream velocity, and in Fig. 4(b) there exists a nonzero transverse momentum. The tripping of Kelvin-Helmholtz instability [39] is

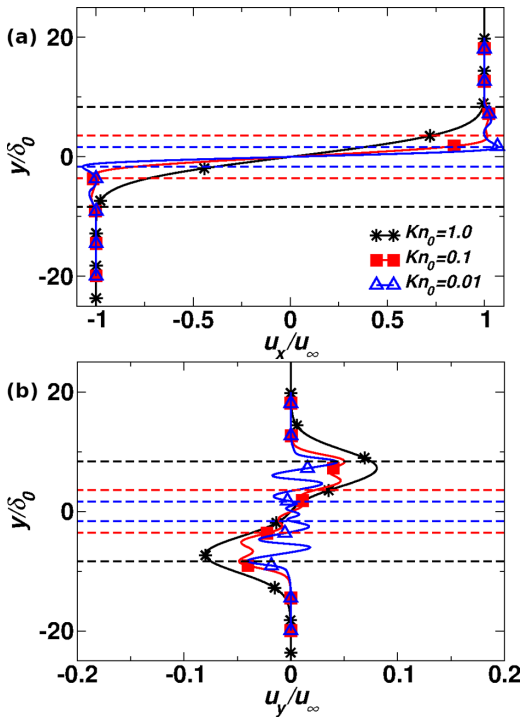


FIG. 6. Variation of (a) $u_x(x = L_x/2, y)$ and (b) $u_y(x = L_x/2, y)$ along $y$ for $\mathrm{Kn}_0 = 0.01$ (blue), $\mathrm{Kn}_0 = 0.1$ (red), and $\mathrm{Kn}_0 = 1$ (black) for $\mathrm{Ma}_c = 1.2$ and $t^* = 10$. The flow variables are normalized by the corresponding freestream values.

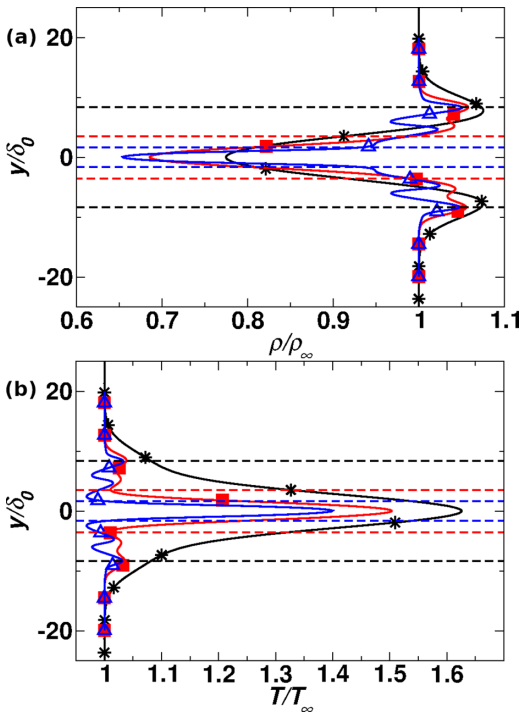


FIG. 7. Variation of (a) $\rho(x = L_x/2, y)$ and (b) $T(x = L_x/2, y)$ for $\mathrm{Kn}_0 = 0.01$ (blue), $\mathrm{Kn}_0 = 0.1$ (red), and $\mathrm{Kn}_0 = 1$ (black) for $\mathrm{Ma}_c = 1.2$ and $t^* = 10$. The flow variables are normalized by the corresponding freestream values. The legend is the same as in Fig. 6.

attributed to the generation of $u_y$ and $u_x$. As $\mathrm{Kn}_0$ increases, the flow stabilizes and $u_y$ becomes negligible. Also, note that in Fig. 5 the perturbations in density and temperature profiles are negligible for this low Mach number as the flow is nearly incompressible. Another remarkable inference is the widening of the mixing layer as $\mathrm{Kn}_0$ increases. At this low $\mathrm{Ma}_c$ as in Fig. 4(b), it can be seen that at large $\mathrm{Kn}_0$ the transverse velocity is minimal. This negligible transverse velocity is due to the density being constant at low $\mathrm{Ma}_c$, as seen in Fig. 5(a). On applying constant density in the mass conservation equation (which remains unaffected by the noncontinuum), it is shown that the transverse velocity should also be constant. Since the transverse velocity is zero far away from the mixing layer, the transverse velocity is zero throughout the mixing layer. In Figs. 6 and 7, at $\mathrm{Ma}_c = 1.2$, the compressibility effects are evident in the velocity distributions. At low $\mathrm{Kn}_0$, the wavelike nature of the perturbations is visible for all the flow variables, as reported by Karimi and Girimaji [40]. These perturbations are present well past the mixing layer width (dashed line), indicating the action of velocity-pressure oscillations beyond the mixed layer. The density and temperature distribution shows variation near the centerline of the mixing layer for all $\mathrm{Kn}_0$, indicating the effect of compressibility at high $\mathrm{Ma}_c$, which is negligible for low $\mathrm{Ma}_c$, as shown in Fig. 5.

The contour distribution of transverse velocity $u_y$ shown in Figs. 8 and 9 highlights the wavelike perturbations due to compressibility. This wavelike nature is seen to weaken with the increase in $\mathrm{Kn}_0$, ultimately becoming nonexistent at $\mathrm{Kn}_0 = 1.0$, as seen in Fig. 9. Instead, at high $\mathrm{Kn}_0$, the mixing layer width increases and shows spreading of the transverse

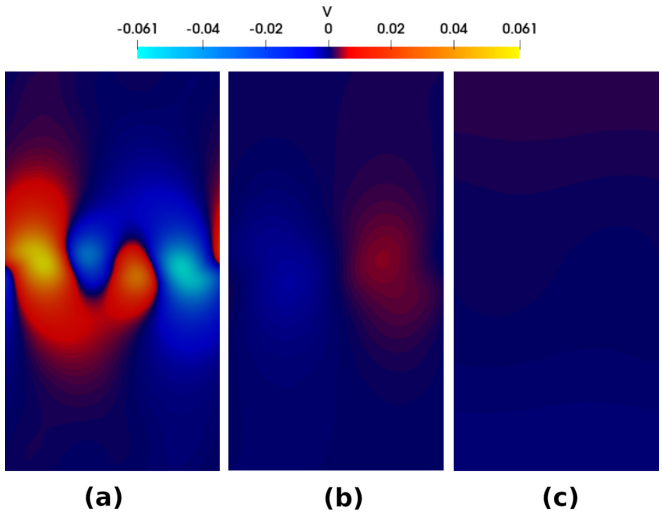


FIG. 8. Transverse velocity $u_y$ contour for $\mathrm{Ma}_c = 0.2$ and $t^* = 10$ for (a) $\mathrm{Kn}_0 = 0.01$, (b) $\mathrm{Kn}_0 = 0.1$, and (c) $\mathrm{Kn}_0 = 1$.

velocity. At low $\mathrm{Ma}_c$, the Kelvin-Helmholtz instability at low $\mathrm{Kn}_0$, shown in Fig. 8(a), disappears at high $\mathrm{Kn}_0$. The absence of transverse velocity perturbations results from the stabilization of the flow.

### B. Comparison of the Boltzmann solution with Grad's 13-moment equations

This section compares the distribution of stress and heat-flux components from computational results with the NSF equations (14) and (15) and Grad's 13-moment equations (18) and (19). The macroscopic quantities and their derivatives are obtained from UGKS simulations of Eq. (2). The NSF and Grad's 13-moment equations are not solved separately. Rather, the terms in Eqs. (14) and (15) and in Eqs. (18) and (19) are obtained from the postprocessing of macroscopic field data from UGKS simulations. Grad's 13-moment

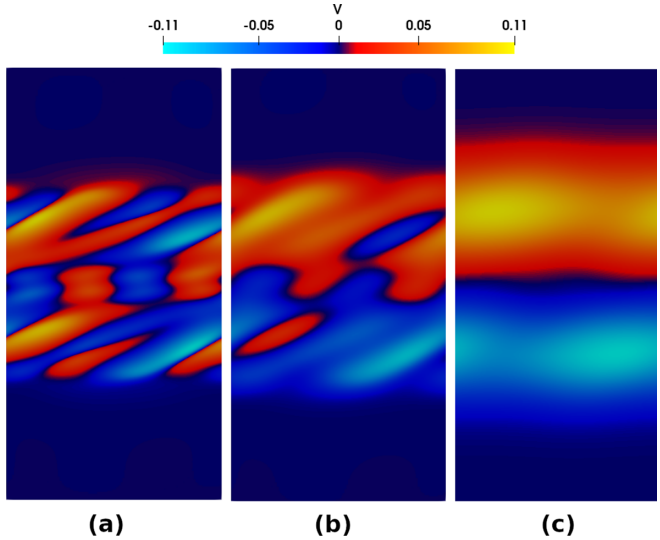


FIG. 9. Transverse velocity $u_y$ contour for $\mathrm{Ma}_c = 1.2$ and $t^* = 10$ for (a) $\mathrm{Kn}_0 = 0.01$, (b) $\mathrm{Kn}_0 = 0.1$, and (c) $\mathrm{Kn}_0 = 1$.

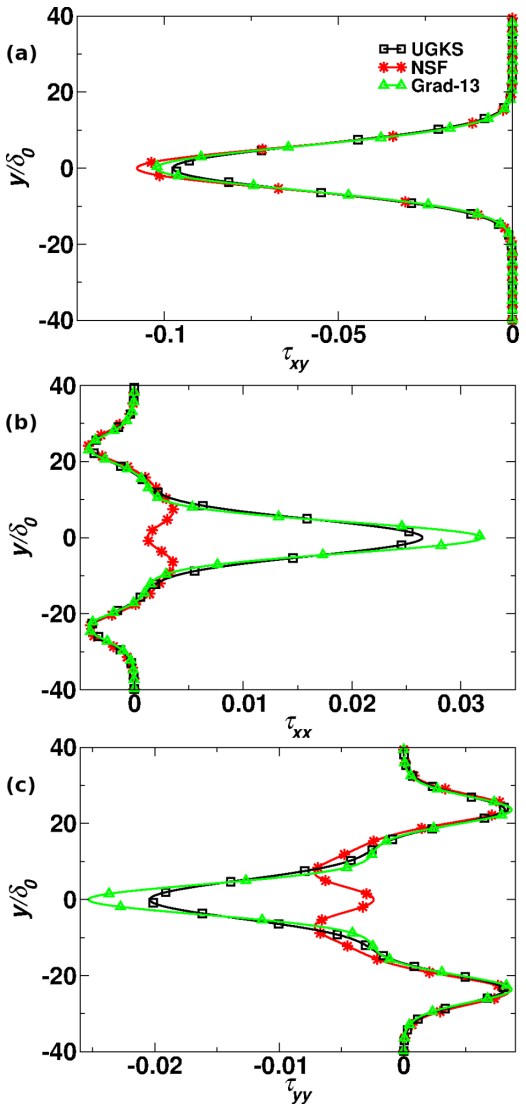


FIG. 10. Comparison of (a) $\tau_{xy}$, (b) $\tau_{xx}$, and (c) $\tau_{yy}$ obtained from moments of the particle distribution function with the Navier-Stokes and Grad's 13-moment equations for $\mathrm{Kn}_0 = 1$, $\mathrm{Ma}_c = 1.2$, and $t^* = 25$.

equations are able to capture nonequilibrium effects much better than the NSF constitutive equations. The NSF equation and Grad's 13-moment equations can be obtained from the BGK-Boltzmann equation by an appropriate expansion of the particle distribution function, as discussed in Sec. II A. While the NSF equation is accurate up to $O(\mathrm{Kn})$, Grad's 13-moment equations are accurate up to $O(\mathrm{Kn}^2)$ [24,25].

Figure 10 shows the distribution of instantaneous streamwise averaged stresses $\tau_{xy}$, $\tau_{yy}$, and $\tau_{xx}$ at $t^* = 25$ for $\mathrm{Ma}_c = 1.2$ and $\mathrm{Kn}_0 = 1.0$. The stresses from the present UGKS simulation are compared with continuum NSF and Grad's 13-moment equations. It can be seen that the maximum deviation from the NSF equation occurs at the center of the mixing layer for all three stresses, where the gradients in the velocity field are maximum. The NSF equation overestimates the magnitude of the $\tau_{xy}$, whereas Grad's 13-moment equations provide better agreement with the computational value. The NSF $\tau_{yy}$ and $\tau_{xx}$ fail to capture the peaks at the center of the mixing layer, while Grad's 13-moment equation overshoots the UGKS Boltzmann solution. Since Grad's 13-moment equation makes corrections to the NSF equation, thus producing better agreement with the computational results, it would be a good model equation to analyze continuum breakdown and kinetic effects.

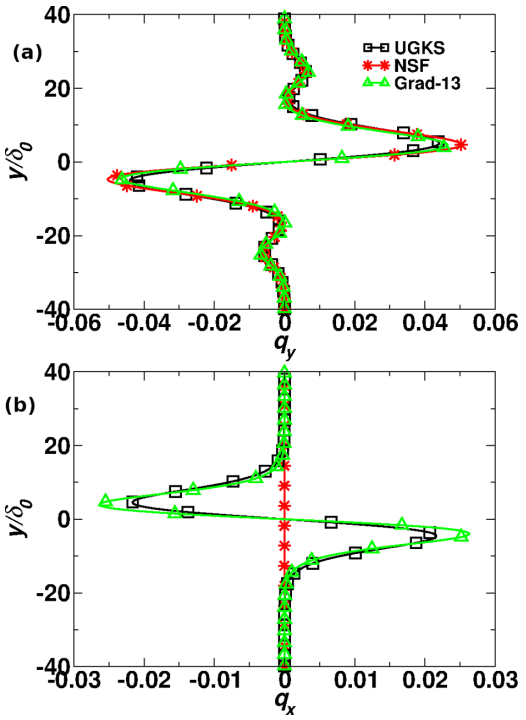


FIG. 11. Comparison of (a) $q_y$ and (b) $q_x$ obtained from moments of the particle distribution function with the NSF and Grad's 13-moment equations for $\mathrm{Kn}_0 = 1$, $\mathrm{Ma}_c = 1.2$, and $t^* = 25$.

The comparison of heat fluxes is shown in Fig. 11. The deviation of the transverse heat flux $q_y$ between the three models is marginal, with Grad's 13-moment equation being closer to the UGKS results. According to the NSF equation, $q_x$ should be uniformly zero throughout the domain; however, UGKS simulations show nonzero $q_x$. Grad's 13-moment equation properly captures this, although it slightly overshoots the computational value, as shown in Fig. 11(b). Unlike the stress components, where the maximum deviation is seen at the center of the mixing layer, the maximum deviation occurs away from the centerline towards the edge of the mixing layer width for the heat-flux components. The nonzero heat flux in the Grad's 13-moment equation is obtained by accounting for spatiotemporal variation of heat flux, stress tensor, and thermodynamic and kinematic variables, allowing Grad's 13-moment equation to capture nonequilibrium phenomenon better than the NSF equation. Comparison of Grad's 13-moment equation and UGKS simulation results shows that Grad's 13-moment equation captures the variation of gas-kinetic stress and heat flux with reasonable accuracy.

### C. Scaling of deviation of $\tau_{xy}$ and $q_y$ from NSF equations

The kinetic effect at continuum breakdown has been quantified using $\mathrm{Kn}\,\mathrm{Ma}_c$ by many early investigators [8,9]. At low

$\mathrm{Ma}_c$, however, this parameter is negligible and thus useless. An alternative method provided by Lockerby *et al.* [15] looked at the $L_2$-norm of the deviation of the stress tensor and heat-flux components. In this section the scaling of shear stress and transverse heat flux with $\mathrm{Kn}_t = \mathrm{Kn}_0\delta_0/\delta(t)$ and $\mathrm{Kn}_t\mathrm{Ma}_c$ is investigated to identify a parameter to quantify the kinetic effects.

In the preceding section it was seen that the peak deviations in stress at the centerline and heat flux occur slightly away from the centerline of the mixing layer. The scaling is done by taking the peak deviations of $\tau_{xy}$ and $q_y$, obtained from the computational results from the NSF equation and normalizing it at each instant of time. The normalization is done using the order of magnitude analysis as

$$O(\tau_{xy}) = O\left(\mu\frac{\partial u_x}{\partial y}\right) = \frac{\mu\Delta u}{\delta}, \tag{24}$$

$$O(q_y) = O\left(\kappa\frac{\partial T}{\partial y}\right) = \frac{\mu\Delta u^2}{\delta}, \tag{25}$$

where $O(RT) = \Delta u^2$, $O(u_x) = \Delta u$, $O(y) = \delta$, and $O(\mu) = O(\kappa/R) = \mu$ [see the discussion pertaining to Eq. (15)]. Temperature is normalized using the Crocco-Busemann relationship, which gives $d^2h/du^2 = -1$, where $h = C_pT$ is enthalpy, for zero streamwise pressure gradient and $\mathrm{Pr} = 1$ [41].

The deviations of $\tau_{xy}$ and $q_y$ are scaled as

$$\Delta_{\tau_{xy}} = \frac{\tau_{xy,B} - \tau_{xy,\mathrm{NS}}}{\mu\Delta u/\delta}, \tag{26}$$

$$\Delta_{q_y} = \frac{q_{y,B} - q_{y,\mathrm{NS}}}{\mu\Delta u^2/\delta}. \tag{27}$$

The real distribution function for mixing layers at $t^* = 0$ is not known beforehand. The flow is assumed to be in local equilibrium in the domain, which can be utilized to initialize the particle distribution function. Thus, the Maxwellian equilibrium distribution function is chosen to initialize the flow field. It should be noted that due to the presence of gradients in the flow field, this does not represent a state of global equilibrium. Thus, the particle distribution function evolves from this state. In the present computation, since the flow field is initialized with the equilibrium distribution function, $\tau_{xy,B} = 0$ at $t^* = 0$. Thus, the parameter $\Delta_{\tau_{xy}}$ would be equal to unity at $t^* = 0$ from Eqs. (24) and (26).

Figures 12(a) and 12(b) plot the maximum deviation of normalized shear stress against $\mathrm{Kn}_t$ and $\mathrm{Kn}_t\mathrm{Ma}_c$, respectively. As shown in Fig. 12(a), the deviation of shear stress from the NSF constitutive equation increases with an increase in $\mathrm{Kn}_t$, as well as with an increase in $\mathrm{Ma}_c$. As $\mathrm{Ma}_c \to 0$, the deviation of shear stress is nearly independent of $\mathrm{Ma}_c$, as the red and the black (bottom two) curves in Fig. 12(a) almost coincide. However, as $\mathrm{Ma}_c$ increases, the deviation depends on $\mathrm{Ma}_c$. The deviation of shear stress at higher $\mathrm{Ma}_c$ follows $\mathrm{Ma}_c\mathrm{Kn}_t$ scaling, as seen from Fig. 12(b), where the curves of the deviations all cluster together. Intermediate values of $\mathrm{Ma}_c$, given by the green ($\mathrm{Ma}_c = 0.3$), blue ($\mathrm{Ma}_c = 0.4$), and brown curves ($\mathrm{Ma}_c = 0.5$), show neither the high-$\mathrm{Ma}_c$ nor the low-$\mathrm{Ma}_c$ behavior, as can be seen in both Figs. 12(a) and 12(b). These cases act as transitions between the low-$\mathrm{Ma}_c$ and the high-$\mathrm{Ma}_c$

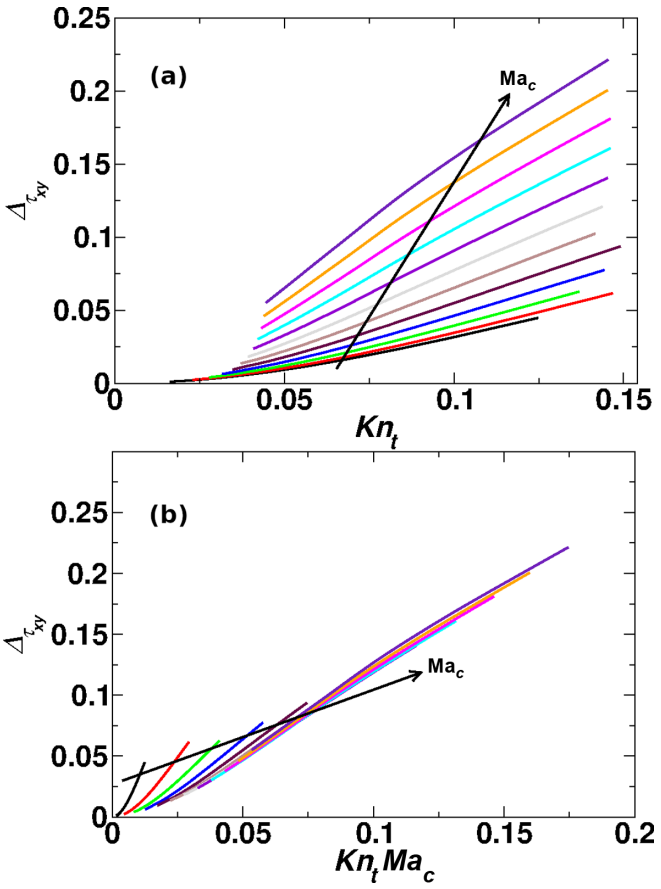


FIG. 12. Maximum deviation of the shear stress $\tau_{xy,B}$ from the Navier-Stokes constitutive equation, $\tau_{xy,\mathrm{NS}}$, with (a) $\mathrm{Kn}_t$ and (b) $\mathrm{Ma}_c\mathrm{Kn}_t$ for different values of $\mathrm{Ma}_c$ and $\mathrm{Kn}_0 = 1.0$.

scaling. The inference from Fig. 12 is that for $\tau_{xy}$, there exist three scalings, namely, at low $\mathrm{Ma}_c$, $\Delta_{\tau_{xy}} \sim \mathrm{Kn}_t$ [Fig. 12(a)]; at high $\mathrm{Ma}_c$, $\Delta_{\tau_{xy}} \sim \mathrm{Kn}_t\mathrm{Ma}_c$ [Fig. 12(b)]; and at intermediate $\mathrm{Ma}_c$ [Fig. 12(c)], which shows behavior intermediate to the previous two scaling.

A similar inference can be obtained for the $q_y$ scaling from Figs. 13(a) and 13(b). The magnitude of the deviation of $q_y$ from continuum is one order lower than that of $\tau_{xy}$. It should be noted that $\Delta_{\tau_{xy}}$ and $\Delta_{q_y}$ in Figs. 12 and 13 are global measures of the deviation of kinetic shear stress and transverse heat flux from the NSF equation.

The physical interpretation of $\mathrm{Kn}_t\mathrm{Ma}_c$ can be obtained by rearranging the terms as follows:

$$\mathrm{Ma}_c\mathrm{Kn} = \frac{\Delta u}{2a}\frac{\lambda}{\delta} = \frac{\lambda/a}{2\delta/\Delta u}. \tag{28}$$

It can be seen from Eq. (28) that at large $\mathrm{Ma}_c$, continuum breakdown depends on the ratio of the microscopic timescale (given by $\lambda/a$) to the macroscopic timescale ($2\delta/\Delta u$), unlike Kn, which is the ratio of the length scales. It can be inferred that while at low $\mathrm{Ma}_c$ the length scales are important, at high $\mathrm{Ma}_c$ timescales play an important role in determining the deviation of $\tau_{xy}$ and $q_y$ from the NSF equation.

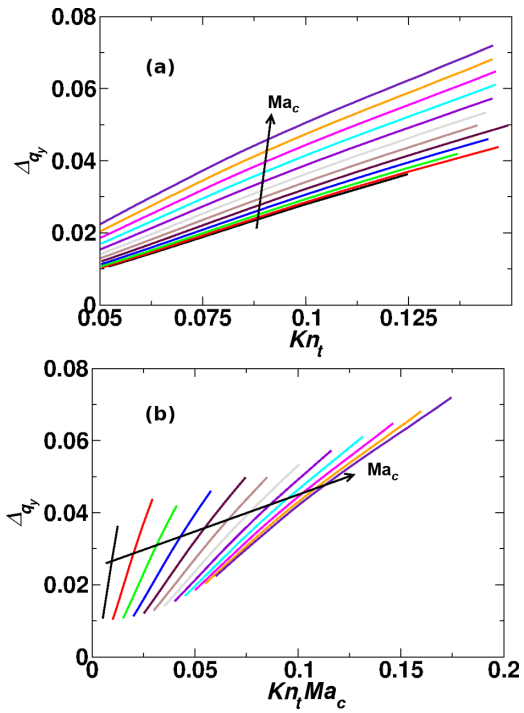


FIG. 13. Maximum deviation of the heat-flux vector $q_{y,B}$ from the Navier-Stokes constitutive equation, $q_{y,\mathrm{NS}}$, with (a) $\mathrm{Kn}_t$ and (b) $\mathrm{Ma}_c\mathrm{Kn}_t$ for different values of $\mathrm{Ma}_c$ and $\mathrm{Kn}_0 = 1.0$.

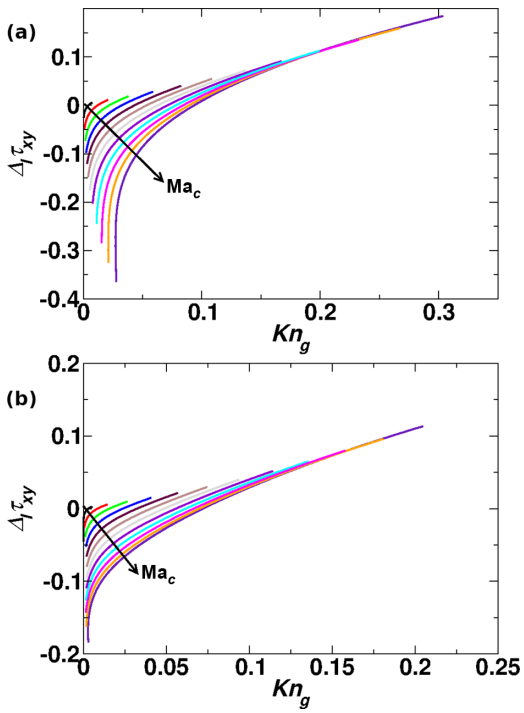


FIG. 14. Plot of the local deviation of the shear stress $\Delta_l\tau_{xy}$ against $\mathrm{Kn}_g$ for different $\mathrm{Ma}_c$ and $\mathrm{Kn}_0 = 1$ at (a) $t^* = 10$ and (b) $t^* = 20$.

#### 1. *Local scaling for high-Mach-number flows*

In the continuum regime, due to the elliptical nature of the incompressible NSF equation, information about changes in the flow field is instantaneously available throughout the entire flow domain. However, at high Mach numbers, the NSF equation becomes hyperbolic, such that only certain regions in the flow field have information about changes in a particular point (zone of action). In contrast, the remaining regions do not get that information (zone of silence). Moreover, the Poisson equation is solved in incompressible solvers, which requires information about the entire flow field, whereas only local flow variables are needed in compressible solvers. This indicates that a global scaling of deviation from the NSF equation would be sufficient in the low-Mach-number limit, whereas in the high-Mach-number limit a local scaling would be better than the global scaling, as evident from Figs. 12 and 13 in the preceding section.

The objective of this section is to define the local equivalents of $\Delta_{\tau_{xy}}$, $\Delta_{q_y}$, and $\mathrm{Kn}_t\mathrm{Ma}_c$, which are checked for scaling. The local equivalent of the above variables are suggested as

$$\Delta_l\tau_{xy}(y) = \frac{\tau_{xy,\mathrm{NSF}} - \tau_{xy,B}}{\tau_{xy,\mathrm{NSF}}}, \tag{29}$$

$$\Delta_l q_y(y) = \frac{q_{y,\mathrm{NSF}} - q_{y,B}}{q_{y,\mathrm{NSF}}}, \tag{30}$$

$$\mathrm{Kn}_g(y) = \frac{\partial}{\partial y}\left(\frac{\lambda u_x}{a}\right), \tag{31}$$

where $\lambda = (\mu/p)\sqrt{\pi RT/2}$ [42,43]. The relationship between the gradient Knudsen number $\mathrm{Kn}_g$ and $\mathrm{Kn}_t\mathrm{Ma}_c$ is analogous to the relationship between the convective Mach number $\mathrm{Ma}_c$ and gradient Mach number $\mathrm{Ma}_g = (\partial u/\partial y)/ka$ ($k$ is the wave number of the perturbation considered), defined in continuum compressible mixing layers [40,44]. A high value of $\mathrm{Kn}_t\mathrm{Ma}_c$ would correspond to a high value of the gradient Knudsen number due to the large gradients of field variables generated in the flow.

A comparison of $\mathrm{Kn}_g$ with $\mathrm{Kn}_{GLL}$ defined by Boyd *et al.* [12] demonstrates the effectiveness of the present definition. Boyd *et al.* [12] defined $\mathrm{Kn}_{GLL} = (\lambda/Q)|\nabla Q|$, where $Q$ can be either temperature or density. The $\mathrm{Kn}_{GLL}$ is a special case of $\mathrm{Kn}_g$, as can be seen by expanding Eq. (31) as

$$\mathrm{Kn}_g = \frac{u_x}{a}\frac{\partial\lambda}{\partial y} + \frac{\lambda}{a}\frac{\partial u_x}{\partial y} - \frac{\lambda u_x}{a^2}\frac{\partial a}{\partial y}. \tag{32}$$

By taking $a = \sqrt{\gamma RT}$, the third term on the right-hand side can be further simplified as

$$\frac{\lambda u_x}{a^2}\frac{\partial a}{\partial y} = \frac{\lambda u_x}{\sqrt{\gamma R}}\frac{1}{T^{3/2}}\frac{\partial T}{\partial y}. \tag{33}$$

Equation (33) is of the form of $\mathrm{Kn}_{GLL}$. In the case not accounting for the variations of $u_x$ and $\lambda$ in space, Eq. (32) reduces to the form of $\mathrm{Kn}_{GLL}$.

From Eq. (32) it is evident that there are three scales which play an essential role in determining the magnitude of the kinetic effects. These are based on the gradient of the mean-free path, velocity, and temperature. The discussion that follows correlates the quantities in Eqs. (29) and (30) with $\mathrm{Kn}_g$ and $\mathrm{Kn}_{GLL}$.

Figure 14 shows the variation of $\Delta_l\tau_{xy}(y)$ as a function of $\mathrm{Kn}_g(y)$ at two representative instances $t^* = 10$ and 20. Since $\tau_{xy,\mathrm{NSF}} = 0$ outside the mixing layer, $\Delta_l\tau_{xy}$ would be

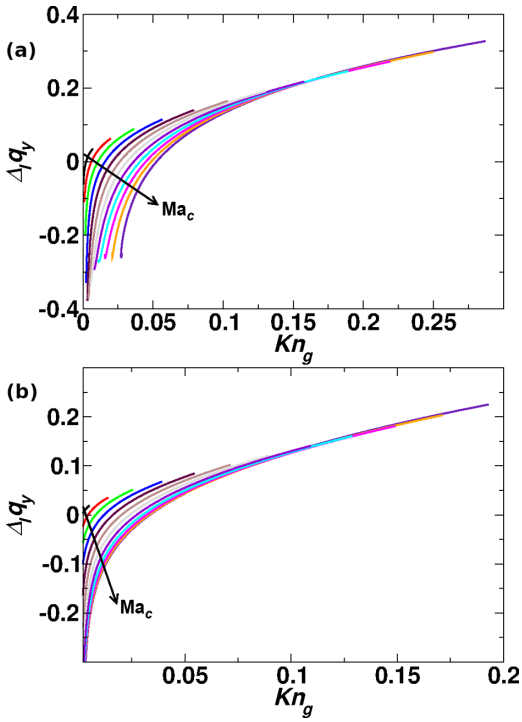


FIG. 15. Plot of the local deviation of the transverse heat flux $\Delta_l q_y$ against $\mathrm{Kn}_g$ for different $\mathrm{Ma}_c$ and $\mathrm{Kn}_0 = 1$ at (a) $t^* = 10$ and (b) $t^* = 20$.

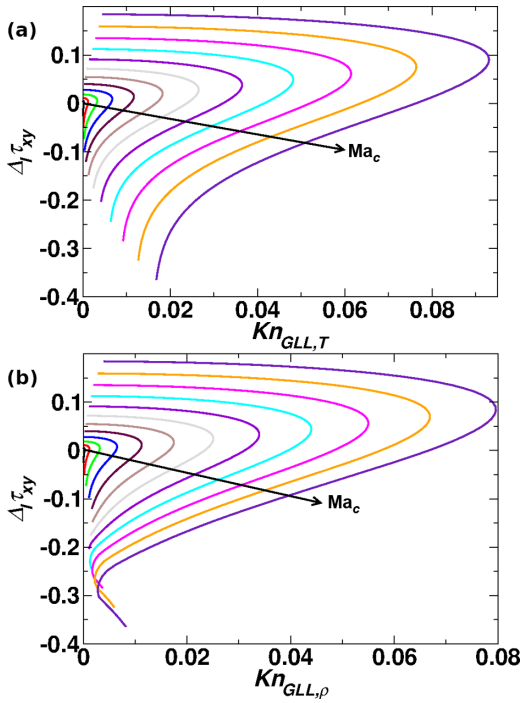


FIG. 16. Plot of the local deviation of the shear stress $\Delta_l \tau_{xy}$ against $\mathrm{Kn}_{GLL}$ based on (a) temperature and (b) density for different $\mathrm{Ma}_c$ at $t^* = 10$.

undefined; thus $\Delta_l \tau_{xy}$ and $\mathrm{Kn}_g$ are evaluated for $y \in (-\delta, \delta)$. It can be seen from Fig. 14 that as $\mathrm{Kn}_g$ increases, $\Delta_l \tau_{xy}$ also increases. As $\mathrm{Ma}_c$ increases, the curves shift towards the right, which implies that an increase in $\mathrm{Ma}_c$ leads to an increase in $\mathrm{Kn}_g$. For low values of $\mathrm{Kn}_g$, $\Delta_l \tau_{xy}$ calculated for different values of $\mathrm{Ma}_c$ follows different curves. However, at high $\mathrm{Kn}_g$, $\Delta_l \tau_{xy}$ is a function of $\mathrm{Kn}_g$ only. This is because the global scaling with $\mathrm{Kn}_t \mathrm{Ma}_c$ obtained only works at large values of $\mathrm{Ma}_c$, as was observed previously in Fig. 12, which would correspond to high values of $\mathrm{Kn}_g$.

Similarly, Fig. 15 shows the variation of $\Delta_l q_y$ with $\mathrm{Kn}_g$ for $t^* = 10$ and 20. The $\Delta_l q_y$ becomes undefined outside the shear layer and at the center of the shear layer, where the temperature peaks ($\partial T/\partial y = 0$). Thus, $\Delta_l q_y$ is only calculated for $|y| \in (0.1\delta, \delta)$. Conclusions similar to those regarding $\Delta_l \tau_{xy}$ can also be drawn for $\Delta_l q_y$. In short, as the deviations from the NSF equation, represented as $\Delta_l \tau_{xy}$ and $\Delta_l q_y$, increase, the parameter $\mathrm{Kn}_g$ also increases.

Figures 16 and 17 show the variations of $\Delta_l \tau_{xy}(y)$ and $\Delta_l q_y(y)$, respectively, against $\mathrm{Kn}_{GLL}$ at $t^* = 10$. The $\mathrm{Kn}_{GLL}$ can be computed by either substituting $Q = T$, shown in Figs. 16(a) and 17(a), or by substituting $Q = \rho$, shown in Figs. 16(b) and 17(b). It can be seen in both figures that neither of the two methods to compute $\mathrm{Kn}_{GLL}$ shows any reasonable scaling for $\Delta_l \tau_{xy}$ or $\Delta_l q_y$. It is seen that as $\mathrm{Ma}_c$ increases, the range of values covered by $\mathrm{Kn}_{GLL}$, $\Delta_l \tau_{xy}$ and $\Delta_l q_y$ also increases. The deviations from the NSF equation, namely, $\Delta_l \tau_{xy}$ and $\Delta_l q_y$, are nonmonotonic with $\mathrm{Kn}_{GLL}$, unlike the monotonically increasing behavior noted with $\mathrm{Kn}_g$. Thus, it is concluded that $\mathrm{Kn}_{GLL}$ is not a reliable parameter to identify continuum breakdown and to characterize the deviations from the NSF equation.

In the present section it is observed that the local equivalents of $\Delta_{\tau_{xy}}$, $\Delta_{q_y}$, and $\mathrm{Kn}_t \mathrm{Ma}_c$ are able to accurately characterize the local deviation from continuum. The gradient Knudsen number, the local equivalent of $\mathrm{Kn}_t \mathrm{Ma}_c$, provides a good scaling for the local deviation of shear stress and transverse heat flux at high values.

### D. Scaling of deviation of $\tau_{yy}$, $\tau_{xx}$, and $q_x$ from the NSF equation

In this section the scaling of the deviation of $\tau_{yy}$, $\tau_{xx}$, and $q_x$ from the NSF equation with respect to $\mathrm{Kn}_t$ and $\mathrm{Kn}_t \mathrm{Ma}_c$ is studied. This is done to check whether all stress tensor and heat-flux components scale comparably. Similar to the preceding section, the peak deviation is considered for the scaling. The normalization is done using the argument that

$$O(\tau_{yy}) = O(\tau_{xx}) = O\left(\mu \frac{\partial u_y}{\partial y}\right) = \frac{\mu^2}{\rho_\infty \delta^2}. \tag{34}$$

The scaling for the transverse velocity $u_y$ is obtained by using the boundary layer assumption (viscous and advective forces balance each other) and the mass conservation equation, which gives $O(u_y) = \mu/\rho_\infty \delta$.

The stress component $\tau_{yy}$ plays an important role in the development of rarefied mixing layers by contributing to viscous force in the $y$ momentum ($\partial \tau_{yy}/\partial y$) and viscous heating in the energy equation [$\tau_{yy}(\partial u_y/\partial y)$]. The normalization of $\tau_{yy}$ and $\tau_{xx}$, given by $\Delta_{\tau_{yy}}$ and $\Delta_{\tau_{xx}}$, respectively, is similar to Eq. (26) with the denominator replaced by $\mu^2/\rho_\infty \delta^2$. Figure 18 shows $\Delta_{\tau_{yy}}$ as a function of $\mathrm{Kn}_t$ and $\mathrm{Kn}_t \mathrm{Ma}_c$. Figure 18(a) shows

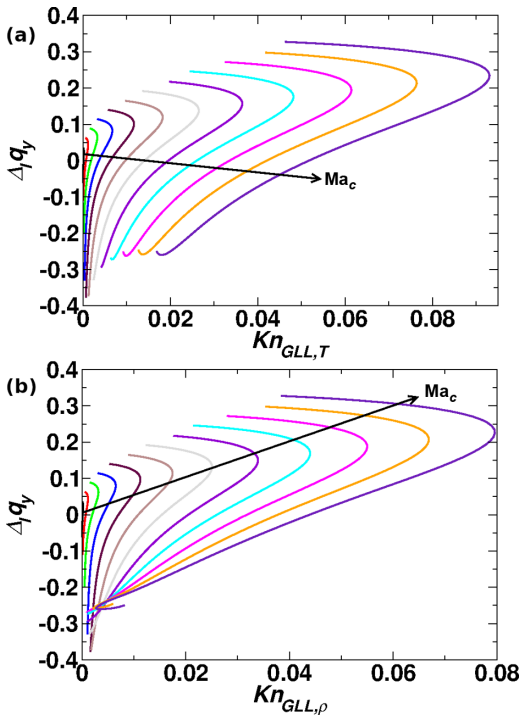


FIG. 17. Plot of the local deviation of the transverse heat flux $\Delta_l q_y$ against $\mathrm{Kn}_{GLL}$ based on (a) temperature and (b) density for different $\mathrm{Ma}_c$ at $t^* = 10$.

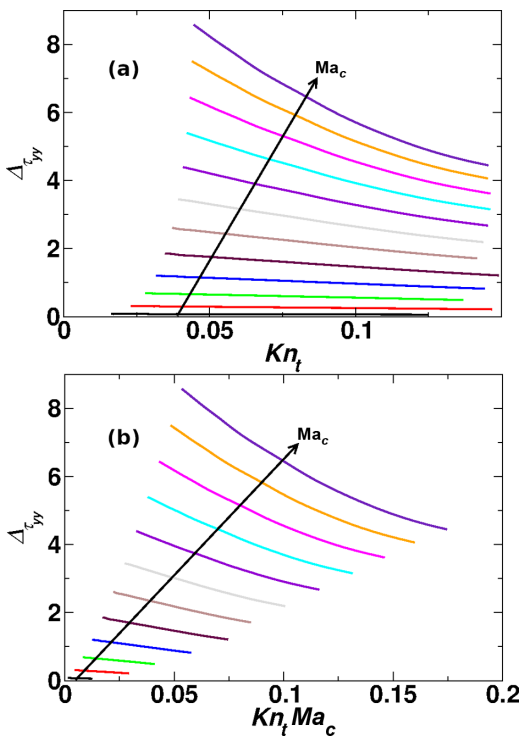


FIG. 18. Maximum deviation of the normal stress $\tau_{yy,B}$ from the Navier-Stokes constitutive equation $\tau_{yy,\mathrm{NS}}$ with (a) $\mathrm{Kn}_t$ and (b) $\mathrm{Ma}_c\mathrm{Kn}_t$ for different values of $\mathrm{Ma}_c$ and $\mathrm{Kn}_0 = 1.0$.

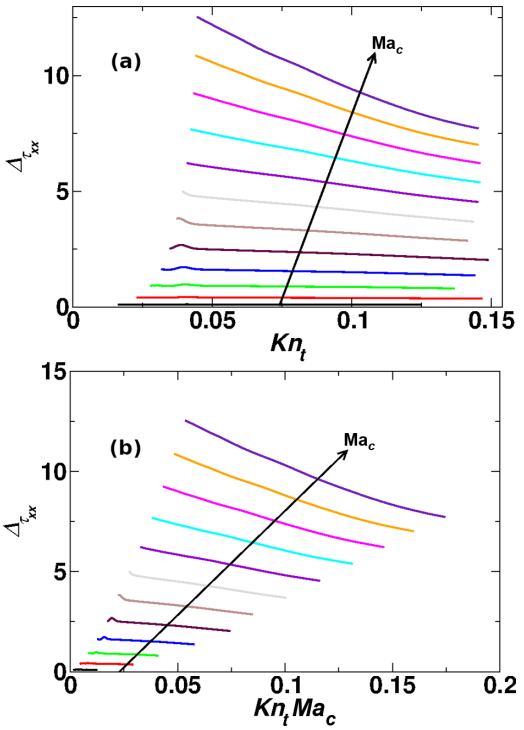


FIG. 19. Maximum deviation of the normal stress $\tau_{xx,B}$ from the Navier-Stokes constitutive equation $\tau_{xx,\mathrm{NS}}$ with (a) $\mathrm{Kn}_t$ and (b) $\mathrm{Ma}_c\mathrm{Kn}_t$ for different values of $\mathrm{Ma}_c$ and $\mathrm{Kn}_0 = 1.0$.

that $\Delta_{\tau_{yy}}$ increases as $\mathrm{Ma}_c$ increases and decreases as $\mathrm{Kn}_t$ increases. The latter trend, which is different from what is seen for $\Delta_{\tau_{xy}}$, is due to the denominator of $\Delta_{\tau_{yy}}$, i.e., $\mu^2/\rho_\infty\delta^2$, approaching zero faster than the numerator, i.e., $\tau_{yy,B} - \tau_{yy,\mathrm{NS}}$, as $\mathrm{Kn}_t$ decreases. Figure 18(a) shows that at low $\mathrm{Ma}_c$, $\Delta_{\tau_{yy}}$ depends only on $\mathrm{Kn}_t$, as can be seen by the proximity of the red and black curves. From Fig. 18(b) it is inferred that the term $\mathrm{Kn}_t\mathrm{Ma}_c$ does not play an important role in $\Delta_{\tau_{yy}}$; instead, both $\mathrm{Kn}_t$ and $\mathrm{Ma}_c$ individually contribute to this deviation. Thus, it is deduced that $\tau_{yy}$ and $\tau_{xx}$ shows two modes of scaling, at low $\mathrm{Ma}_c$, where $\Delta_{\tau_{yy}} \sim \mathrm{Kn}_t$ [Fig. 18(a)], and at high $\mathrm{Ma}_c$, where $\Delta_{\tau_{yy}} \sim f(\mathrm{Kn}_t, \mathrm{Ma}_c)$ [Fig. 18(b)]. Similar conclusions can be drawn for $\Delta_{\tau_{xx}}$, from Figs. 19(a) and 19(b). In Sec. III B it was shown that, even though the NSF equation gives $q_x = 0$, a nonzero value of $q_x$ is obtained from computational results and that Grad's 13-moment equation is able to reproduce the computational result better. In order to normalize the deviation of $q_x$ from the NSF equation, a noncontinuum term in Grad's 13-moment equation is chosen, namely, $(\tau_{xy}/\rho v)(\partial\tau_{yy}/\partial y)$, and is normalized using the equation

$$\Delta_{q_x} = \frac{q_{x,B} - q_{x,\mathrm{NS}}}{\lambda\mu^3 u_\infty/a_\infty\rho_\infty^2\delta^4}. \tag{35}$$

Here $O(v) = a_\infty/\lambda$, where $a_\infty$ is the freestream speed of sound, which is of the same order of magnitude as the molecular speeds, $u_\infty = \Delta u/2$ is the freestream velocity, and $\lambda$ is the mean-free path of the medium. Figure 20(a) shows that, similar to $\Delta_{\tau_{xx}}$ and $\Delta_{\tau_{yy}}$, $\Delta_{q_x}$ decreases with an increase in $\mathrm{Kn}_t$ but increases with $\mathrm{Ma}_c$. Similar to $\Delta_{\tau_{yy}}$ and $\Delta_{\tau_{xx}}$, as $\mathrm{Kn}_t$ decreases, the denominator in $\Delta_{q_x}$ decrease faster in

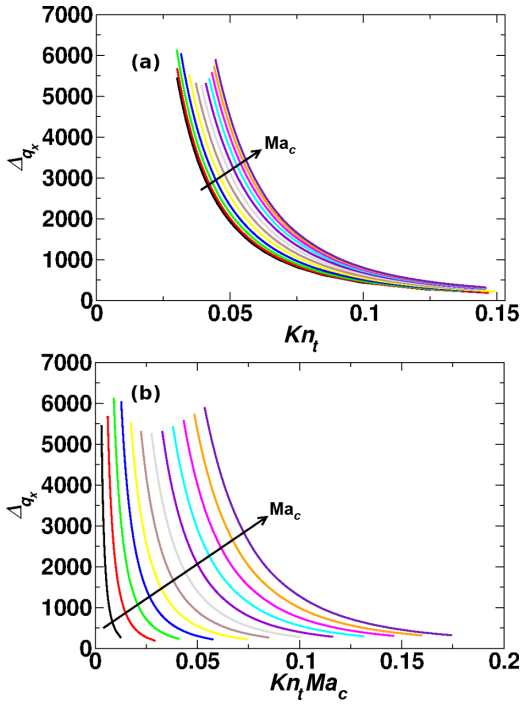


FIG. 20. Maximum deviation of the normal stress $q_{x,B}$ from the Navier-Stokes constitutive equation $q_{x,\mathrm{NS}}$ with (a) $\mathrm{Kn}_t$ and (b) $\mathrm{Ma}_c\mathrm{Kn}_t$ for different values of $\mathrm{Ma}_c$ and $\mathrm{Kn}_0 = 1.0$.

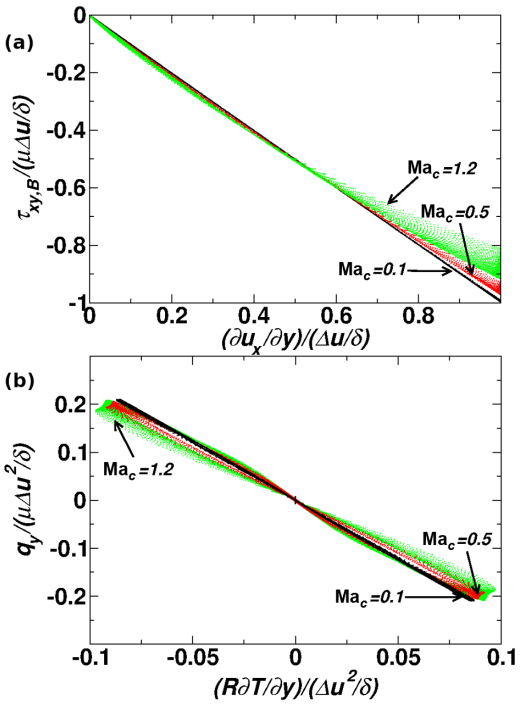


FIG. 21. Scatter plot of (a) normalized $\tau_{xy,B}$ against normalized $\partial u_x/\partial y$ and (b) normalized $q_{y,B}$ against normalized $\partial T/\partial y$ for $\mathrm{Ma}_c = 0.1$ (black), 0.5 (red), and 1.2 (green) for $\mathrm{Kn}_0 = 1$ at various times.

comparison to the numerator; hence the value of $\Delta_{q_x}$ increases with decrease in $\mathrm{Kn}_t$.

It is inferred from the present section that the deviation of $\tau_{xx}$, $\tau_{yy}$, and $q_x$ from the NSF equation shows characteristics different from the deviation observed for $\tau_{xy}$ and $q_y$.

### E. Notion of effective viscosity in the rarefied regime

A study by Ou and Chen [43] on Couette flow in the rarefied regime analyzed the effective viscosity and effective thermal conductivity. However, they looked only at shear stress and transverse heat flux in the study. The present section shows that effective viscosity and conductivity would not be a reliable approach to analyze rarefied regimes. Figure 21 shows the variation of normalized $\tau_{xy,B}$ against normalized $\partial u_x/\partial y$ [Fig. 21(a)] and normalized $q_{y,B}$ against normalized $\partial T/\partial y$ [Fig. 21(b)] for $\mathrm{Ma}_c = 0.1$, 0.5, and 1.2, with $\mathrm{Kn}_0 = 1.0$ over a range of time in the evolution of mixing layer. These variables have been averaged in the streamwise direction as the flow is streamwise homogeneous. It can be seen in Figs. 21(a) and 21(b) that there is a linear dependence of $\partial u_x/\partial y$ on $\tau_{xy,B}$ and $\partial T/\partial y$ on $q_{y,B}$ at low $\mathrm{Ma}_c$; however, there is a considerable spread in the data at high $\mathrm{Ma}_c$. The spread decreases with a decrease in $\mathrm{Ma}_c$. The spread is caused by kinetic effects discerned as the deviation from the NSF equation in the rarefied regime, which has been shown to be more at high $\mathrm{Ma}_c$ in Secs. III C and III D. In order to elucidate the spread of data seen in Fig. 21, the effective viscosity $\mu_{\mathrm{eff}}$ is plotted against the gradient of streamwise velocity and temperature. Figure 22 plots the normalized effective viscosity $\mu_{\mathrm{eff}}/\mu$ against $\partial u_x\partial y$ [Fig. 22(a)] and $\partial T/\partial y$ [Fig. 22(b)]. Effective viscosity can be calculated in two ways,

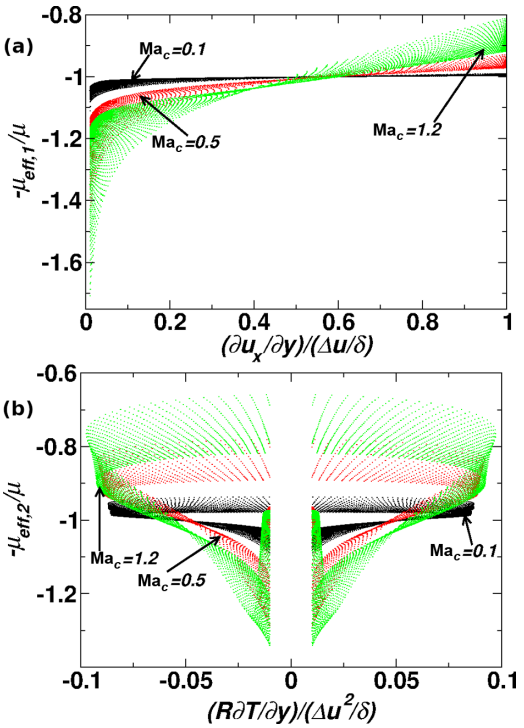


FIG. 22. Scatter plot of the normalized effective viscosity (a) $\mu_{\mathrm{eff},1}/\mu$ obtained from $\tau_{xy}$ and $\partial u_x/\partial y$ against normalized $\partial u_x/\partial y$ and (b) $\mu_{\mathrm{eff},2}/\mu$ obtained from $q_y$ and $\partial T/\partial y$ against normalized $\partial T/\partial y$ for $\mathrm{Ma}_c = 0.1$ (black), 0.5 (red), and 1.2 (green) and $\mathrm{Kn}_0 = 1$ at various times.

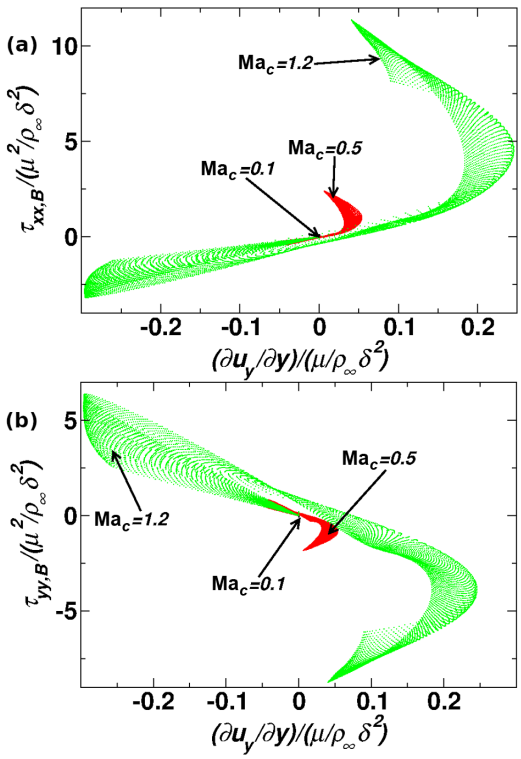


FIG. 23. Scatter plot of (a) normalized $\tau_{xx,B}$ against normalized $\partial u_y/\partial y$ and (b) normalized $\tau_{yy,B}$ against normalized $\partial u_y/\partial y$ for $\mathrm{Ma}_c = 0.1$ (black), 0.5 (red), and 1.2 (green) and $\mathrm{Kn}_0 = 1$ at various times.

by taking (i) the ratio of $\tau_{xy}$ to $\partial u_x/\partial y$, indicated as $\mu_{\mathrm{eff},1}$, or (ii) the ratio of $q_y$ to $\partial T/\partial y$, indicated as $\mu_{\mathrm{eff},2}$. The second method gives effective conductivity $\kappa_{\mathrm{eff}}$ and since $\mathrm{Pr} = 1$, $\mu_{\mathrm{eff},2}$ can be obtained from the relation $\mu_{\mathrm{eff},2} = 2\kappa_{\mathrm{eff}}/5R$ [14]. Figure 22 shows that for $\mathrm{Ma}_c = 0.1$, $\mu_{\mathrm{eff}}/\mu \approx 1$ with only a slight spread in its value (here $\mu_{\mathrm{eff}}$ implies effective viscosity calculated from both methods). However, as $\mathrm{Ma}_c$ increases, the value of $\mu_{\mathrm{eff}}/\mu$ deviates from 1 and there is a considerable spread in the plot. The spread in the value of $\mu_{\mathrm{eff},2}/\mu$ in Fig. 22(b) is more than the spread of $\mu_{\mathrm{eff},1}/\mu$ seen in Fig. 22(a). This increase in the spread for Fig. 22(b) is due to the larger deviation in $q_y$ from the NSF equation. Comparing Figs. 14 and 15, it is evident that $\tau_{xy}$ has a smaller deviation from the NSF equation compared to $q_y$. Note that Eqs. (29) and (30) can be also be written as $\Delta_l \tau_{xy} = 1 - \mu_{\mathrm{eff},1}/\mu$ and $\Delta_l q_y = 1 - \kappa_{\mathrm{eff}}/\kappa$, respectively; thus a large deviation in $\mu_{\mathrm{eff},2}/\mu$ compared to $\mu_{\mathrm{eff},1}/\mu$ is apparent. On changing the $x$ axis to $\mathrm{Kn}_g$ instead of gradients of streamwise velocity or temperature, a better collapse in data can be obtained, which was plotted earlier in Figs. 14 and 15.

Figure 23 shows the variation of normalized $\tau_{xx,B}$ [Fig. 23(a)] and normalized $\tau_{yy,B}$ [Fig. 23(b)] against normalized $\partial u_y/\partial y$ for $\mathrm{Ma}_c = 0.1$, 0.5, and 1.2, at $\mathrm{Kn}_0 = 1.0$ over a range of time. It can also be seen in Figs. 23(a) and 23(b) that $\partial u_y/\partial y$ does not uniquely map to $\tau_{xx,B}$ and $\tau_{yy,B}$, implying that other variables play an important role in the calculation of $\tau_{xx,B}$ and $\tau_{yy,B}$, as given in Eq. (18). Indeed, Figs. 10(b) and 10(c) show that $\tau_{xx,\mathrm{NSF}}$ and $\tau_{yy,\mathrm{NSF}}$ have a different profile from $\tau_{yy,B}$ and $\tau_{xx,B}$ as $y$ approaches the center of the mixing layer. It is tempting to use the minimal spread of the data in Figs. 21(a) and 21(b) to evaluate an effective viscosity and thermal conductivity [43], but such an attempt is futile, as can be seen from the scatter in Fig. 23. Further, an effective conductivity cannot result in a nonzero value of streamwise heat flux $q_x$ since the temperature gradient in the streamwise direction is zero.

## IV. CONCLUSION

Gas-kinetic (UGKS) simulations of rarefied compressible mixing layers were performed to investigate continuum breakdown and the resulting effect on the flow physics. Momentum and thermal transport were examined at various Knudsen and Mach numbers. Most notably, at low Mach numbers, the classical continuum Kelvin-Helmholtz instability was stabilized with increasing Knudsen number due to significant reduction in the transverse velocity. It is now well known in the literature [40] that compressibility effects suppress the Kelvin-Helmholtz instability in the continuum high-Mach-number regime due to wavelike pressure-velocity interactions. The wave behavior diminishes with increasing Knudsen numbers (at high Mach numbers). The transverse velocity remains significant due to density variations. However, the flow remains stable.

In low- and high-speed regimes, the gas-kinetic momentum and thermal transport exhibit marked departures from NSF values. In the low-Mach-number regime, the departure of shear stress and transverse heat flux scales with $\mathrm{Kn}_t$, whereas, at high Mach number it follows $\mathrm{Kn}_t\mathrm{Ma}_c$. At intermediate Mach number, this deviation scales independently with $\mathrm{Kn}_t$ and $\mathrm{Ma}_c$. In general, the deviation of normal stress and streamwise heat flux follows $\mathrm{Kn}_t$ and $\mathrm{Ma}_c$ independently at all Mach numbers.

It was seen that the maximum deviation in the stress tensor occurs at the center of the mixing layer, whereas the peak departure of the heat-flux vector occurs away from it. A dimensionless parameter, the gradient Knudsen number $\mathrm{Kn}_g$, was identified, which characterizes the local departure in shear and heat flux from NSF values. Grad's 13-moment model was shown to capture the qualitative aspects of the noncontinuum effects quite well, even though marked quantitative differences remain. The use of effective viscosity and conductivity as a method to study rarefied flow was tested. A linear relation between $\partial u_x/\partial y$ and $\partial T/\partial y$ with $\tau_{xy,B}$ and $q_{y,B}$ appears plausible at low $\mathrm{Ma}_c$ numbers, but there is considerable spread in data at high $\mathrm{Ma}_c$. Further, the effective viscosity and conductivity paradigm was shown to be unsuitable for normal stress and streamwise heat-flux components.

## ACKNOWLEDGMENTS

We acknowledge the use of the computing resources at HPCE, IIT Madras. The authors are grateful for financial support from the government of India through SPARC Grant No. P805.

[1] A. Rikanati, O. Sadot, G. Ben-Dor, D. Shvarts, T. Kuribayashi, and K. Takayama, Shock-Wave Mach-Reflection Slip-Stream Instability: A Secondary Small-Scale Turbulent Mixing Phenomenon, Phys. Rev. Lett. **96**, 174503 (2006).

[2] D. R. Chapman, Laminar mixing in compressible fluids, NACA Technical notes, NACA-TN-1800 (1949).

[3] J.-L. Wu, Z.-H. Li, A.-P. Peng, X.-C. Pi, and Z.-H. Li, Numerical study on rarefied unsteady jet flow expanding into vacuum using the gas-kinetic unified algorithm, Comput. Fluids **155**, 50 (2017).

[4] R. Kumar, E. V. Titov, D. A. Levin, N. E. Gimelshein, and S. F. Gimelshein, Assessment of Bhatnagar-Gross-Krook approaches for near continuum regime nozzle flows, AIAA J. **48**, 1531 (2010).

[5] S. F. Gimelshein, A. A. Alexeenko, and D. A. Levin, Modeling of the interaction of a side jet with a rarefied atmosphere, J. Spacecr. Rockets **39**, 168 (2002).

[6] V. Venugopal, D. S. Praturi, and S. S. Girimaji, Non-equilibrium thermal transport and entropy analyses in rarefied cavity flows, J. Fluid Mech. **864**, 995 (2019).

[7] H. Akhlaghi, E. Roohi, and S. Stefanov, Ballistic and collisional flow contributions to anti-Fourier heat transfer in rarefied cavity flow, Sci. Rep. **8**, 13533 (2018).

[8] G. A. Bird, Breakdown of translational and rotational equilibrium in gaseous expansions, AIAA J. **8**, 1998 (1970).

[9] H.-S. Tsien, Superaerodynamics, mechanics of rarefied gases, J. Aeronaut. Sci. **13**, 653 (1946).

[10] Y. Ben-Ami and A. Manela, The sound of a pulsating sphere in a rarefied gas: Continuum breakdown at short length and time scales, J. Fluid Mech. **871**, 668 (2019).

[11] H. Struchtrup and M. Torrilhon, Regularization of Grad's 13 moment equations: Derivation and linear analysis, Phys. Fluids **15**, 2668 (2003).

[12] I. D. Boyd, G. Chen, and G. V. Candler, Predicting failure of the continuum fluid equations in transitional hypersonic flows, Phys. Fluids **7**, 210 (1995).

[13] S. Tiwari, Coupling of the Boltzmann and Euler equations with automatic domain decomposition, J. Comput. Phys. **144**, 710 (1998).

[14] H. Struchtrup, *Macroscopic Transport Equations for Rarefied Gas Flows: Approximation Methods in Kinetic Theory* (Springer, Berlin, 2005).

[15] D. A. Lockerby, J. M. Reese, and H. Struchtrup, Switching criteria for hybrid rarefied gas flow solvers, Proc. R. Soc. A **465**, 1581 (2009).

[16] Z. Wang, L. Bao, and B. Tong, Rarefaction criterion and non-Fourier heat transfer in hypersonic rarefied flows, Phys. Fluids **22**, 126103 (2010).

[17] N. Singh and T. E. Schwartzentruber, Heat flux correlation for high-speed flow in the transitional regime, J. Fluid Mech. **792**, 981 (2016).

[18] N. Singh and T. E. Schwartzentruber, Aerothermodynamic correlations for high-speed flow, J. Fluid Mech. **821**, 421 (2017).

[19] M. Macrossan, in *Proceedings of the 25th International Symposium on Rarefied Gas Dynamics*, edited by M. S. Ivanov and A. K. Rebrov (Siberian Branch of the Russian Academy of Sciences, Novosibirsk, 2007), Vol. 1, pp. 759–764.

[20] J.-C. Huang, K. Xu, and P. Yu, A unified gas-kinetic scheme for continuum and rarefied flows II: Multi-dimensional cases, Commun. Comput. Phys. **12**, 662 (2012).

[21] W. G. Vincenti and C. H. Kruger, *Introduction to Physical Gas Dynamics* (Wiley, New York, 1965).

[22] P. L. Bhatnagar, E. P. Gross, and M. Krook, A model for collision processes in gases. I. Small amplitude processes in charged and neutral one-component systems, Phys. Rev. **94**, 511 (1954).

[23] P. K. Kundu and I. M. Cohen, *Fluid Mechanics* (Elsevier, Amsterdam, 2002).

[24] H. Struchtrup, Stable transport equations for rarefied gases at high orders in the Knudsen number, Phys. Fluids **16**, 3921 (2004).

[25] H. Struchtrup, Derivation of 13 moment equations for rarefied gas flow to second order accuracy for arbitrary interaction potentials, Multiscale Model. Simul. **3**, 221 (2005).

[26] L. Mieussens, Discrete-velocity models and numerical schemes for the Boltzmann-BGK equation in plane and axisymmetric geometries, J. Comput. Phys. **162**, 429 (2000).

[27] L. Mieussens, Discrete velocity model and implicit scheme for the BGK equation of rarefied gas dynamics, Math. Models Methods Appl. Sci. **10**, 1121 (2000).

[28] G. A. Bird, *Molecular Gas Dynamics and Direct Simulation of Gas Flows* (Clarendon, Oxford, 1994).

[29] K. Xu and J.-C. Huang, A unified gas-kinetic scheme for continuum and rarefied flows, J. Comput. Phys. **229**, 7747 (2010).

[30] K. H. Prendergast and K. Xu, Numerical hydrodynamics from gas-kinetic theory, J. Comput. Phys. **109**, 53 (1993).

[31] G. May, B. Srinivasan, and A. Jameson, An improved gas-kinetic BGK finite-volume method for three-dimensional transonic flow, J. Comput. Phys. **220**, 856 (2007).

[32] K. Xu, M. Mao, and L. Tang, A multidimensional gas-kinetic BGK scheme for hypersonic viscous flow, J. Comput. Phys. **203**, 405 (2005).

[33] G. Kumar, S. S. Girimaji, and J. Kerimo, WENO-enhanced gas-kinetic scheme for direct simulations of compressible transition and turbulence, J. Comput. Phys. **234**, 499 (2013).

[34] S. Arun, A. Sameen, B. Srinivasan, and S. S. Girimaji, Scale-space energy density function transport equation for compressible inhomogeneous turbulent flows, J. Fluid Mech. **920**, A31 (2021).

[35] V. Venugopal and S. S. Girimaji, Unified gas kinetic scheme and direct simulation Monte Carlo computations of high-speed lid-driven microcavity flows, Commun. Comput. Phys. **17**, 1127 (2015).

[36] N. D. Sandham, The effect of compressibility on vortex pairing, Phys. Fluids **6**, 1063 (1994).

[37] S. Arun, A. Sameen, B. Srinivasan, and S. S. Girimaji, Topology-based characterization of compressibility effects in mixing layers, J. Fluid Mech. **874**, 38 (2019).

[38] B. Shizgal, A Gaussian quadrature procedure for use in the solution of the Boltzmann equation and related problems, J. Comput. Phys. **41**, 309 (1981).

[39] V. Mohan, A. Sameen, B. Srinivasan, and S. S. Girimaji, Influence of Knudsen and Mach numbers on Kelvin-Helmholtz instability, Phys. Rev. E **103**, 053104 (2021).

[40] M. Karimi and S. S. Girimaji, Suppression mechanism of Kelvin-Helmholtz instability in compressible fluid flows, Phys. Rev. E **93**, 041102(R) (2016).

[41] F. M. White, *Viscous Fluid Flow* (McGraw-Hill, New York, 2006).

[42] D. A. Lockerby, J. M. Reese, and M. A. Gallis, Capturing the Knudsen layer in continuum-fluid models of nonequilibrium gas flows, AIAA J. **43**, 1391 (2005).

[43] J. Ou and J. Chen, Nonlinear transport of rarefied Couette flows from low speed to high speed, Phys. Fluids **32**, 112021 (2020).

[44] M. Karimi and S. S. Girimaji, Influence of orientation on the evolution of small perturbations in compressible shear layers with inflection points, Phys. Rev. E **95**, 033112 (2017).